

Complex-amplitude Fourier single-pixel imaging via coherent structured illumination

Hong-Yun Hou(侯红云), Ya-Nan Zhao(赵亚楠), Jia-Cheng Han(韩佳成), De-Zhong Cao(曹德忠),Su-Heng Zhang(张素恒), Hong-Chao Liu(刘宏超), and Bao-Lai Liang(梁宝来)

Citation: Chin. Phys. B, 2023, 32 (**6**): 064201. DOI: 10.1088/1674-1056/ac8e9a

Journal homepage: http://cpb.iphy.ac.cn; http://iopscience.iop.org/cpb

What follows is a list of articles you may be interested in

Deep-learning-based cryptanalysis of two types of nonlinear optical cryptosystems

Xiao-Gang Wang(汪小刚) and Hao-Yu Wei(魏浩宇)

Chin. Phys. B, 2022, 31 (**9**): 094202. DOI: 10.1088/1674-1056/ac6331

Imaging a periodic moving/state-changed object with Hadamard-based computational ghost imaging

Hui Guo(郭辉), Le Wang(王乐), and Sheng-Mei Zhao(赵生妹)

Chin. Phys. B, 2022, 31 (**8**): 084201. DOI: 10.1088/1674-1056/ac6498

An apodized cubic phase mask used in a wavefront coding system to extend the depth of field

Lina Zhu(朱丽娜), Fei Li(李飞), Zeyu Huang(黄泽宇), and Tingyu Zhao(赵廷玉)

Chin. Phys. B, 2022, 31 (**5**): 054217. DOI: 10.1088/1674-1056/ac5979

Color-image encryption scheme based on channel fusion and spherical diffraction

Jun Wang(王君), Yuan-Xi Zhang(张沅熙), Fan Wang(王凡), Ren-Jie Ni(倪仁杰), and Yu-Heng Hu(胡玉衡)

Chin. Phys. B, 2022, 31 (**3**): 034205. DOI: 10.1088/1674-1056/ac1b87

Fast Fourier single-pixel imaging based on Sierra-Lite dithering algorithm

Zhen-Yu Liang(梁振宇), Zheng-Dong Cheng(程正东), Yan-Yan Liu(刘严严), Kuai-Kuai Yu(于快快), Yang-Di Hu(胡洋頔)

Chin. Phys. B, 2019, 28 (**6**): 064202. DOI: 10.1088/1674-1056/28/6/064202

Complex-amplitude Fourier single-pixel imaging via coherent structured illumination

Hong-Yun Hou(侯红云)[1], Ya-Nan Zhao(赵亚楠)[1], Jia-Cheng Han(韩佳成)[1], De-Zhong Cao(曹德忠)[2], Su-Heng Zhang(张素恒)[1,†], Hong-Chao Liu(刘宏超)[3,‡], and Bao-Lai Liang(梁宝来)[1,§]

[1] *Hebei Key Laboratory of Optic-Electronic Information and Materials, College of Physics Science & Technology, Hebei University, Baoding* 071002, *China*
[2] *Department of Physics, Yantai University, Yantai* 264005, *China*
[3] *Institute of Applied Physics and Materials Engineering, University of Macau, Avenida da Universidade, Taipa, Macao SAR, China*

(Received 19 April 2022; revised manuscript received 1 August 2022; accepted manuscript online 2 September 2022)

We propose a method of complex-amplitude Fourier single-pixel imaging (CFSI) with coherent structured illumination to acquire both the amplitude and phase of an object. In the proposed method, an object is illustrated by a series of coherent structured light fields, which are generated by a phase-only spatial light modulator, the complex Fourier spectrum of the object can be acquired sequentially by a single-pixel photodetector. Then the desired complex-amplitude image can be retrieved directly by applying an inverse Fourier transform. We experimentally implemented this CFSI with several different types of objects. The experimental results show that the proposed method provides a promising complex-amplitude imaging approach with high quality and a stable configuration. Thus, it might find broad applications in optical metrology and biomedical science.

Keywords: complex-amplitude imaging, single-pixel imaging, Fourier basis scan, coherent structured illumination

PACS: 42.30.–d, 42.30.Kq, 87.63.lt **DOI:** 10.1088/1674-1056/ac8e9a

1. Introduction

An optical field is expressed as a complex-amplitude, which describes both the amplitude and phase of the light wave. Conventional imaging only observes amplitude information, but the important phase information is lost. This is because the photodetector to the human retina only responds to light intensity. Developing an efficient approach to recover the full complex-amplitude of an optical field has been one of the most attractive challenges in modern imaging science. Starting with early Zernike's phase contrast microscopy,[1] various complex-amplitude imaging techniques have been proposed, such as differential interference contrast microscopy,[2] Shack–Hartmann sensing,[3] coherent diffraction imaging,[4,5] digital holography,[6,7] Fourier ptychographic microscopy,[8] lensless ghost imaging,[9–11] and phase imaging techniques based on transport-of-intensity equation.[12]

Single-pixel imaging (SPI) has attracted intensive interest as an innovative computational imaging technique in recent years.[13] SPI allows one to use a single-pixel detector, such as a photodiode, photomultiplier tube (PMT), or single-photon avalanche diode, to capture images with the help of spatial light modulation. It shifts the stage of the spatial sampling away from the image sensor in traditional imaging techniques to the spatial light modulator. The single-pixel detector offers SPI a wide spectral response range, ultra-high sensitivity, precise timing resolution, and an affordable cost. The shift in the stage of spatial sampling allows SPI to facilitate the application of algorithms such as intensity correlation, compressed sensing, orthogonal basis scanning, and deep learning, making the acquisition of spatial information more flexible and efficient. Thus, SPI has been widely exploited for non-visible light imaging,[14–17] multispectral imaging,[18,19] extremely low light imaging,[20,21] three-dimensional imaging,[22,23] and optical encryption.[24–26]

SPI can capture not only intensity images but also complex-amplitude images. Recently, several attempts were made to acquire the complex-amplitude information of objects by using SPI techniques, such as single-pixel diffractive imaging,[27–29] single-pixel wavefront sensing,[30–32] single-pixel ptychography,[33] single-pixel digital holography,[34–39] and single-pixel phase imaging based on common-path interferometry.[40–46] Benefiting from the advantages of SPI, the complex-amplitude single-pixel imaging is becoming a promising imaging modality in the fields of optical microscopy,[40] optical metrology,[45] and biomedical science.[39]

In this paper, we present a novel complex-amplitude Fourier single-pixel imaging (CFSI) method by combining coherent structured illumination[29,35,40,42,45] and common-path interference[40–46] with a Fourier basis scan.[47–51] Different from previous CFSI methods[37,42,44] that use the digital micromirror device (DMD) for complex-amplitude modulation, we employ a phase-only liquid-crystal-on-silicon spatial light

[†]Corresponding author. E-mail: shzhang@hbu.edu.cn
[‡]Corresponding author. E-mail: hcliu@um.edu.mo
[§]Corresponding author. E-mail: liangbaolai@gmail.com

© 2023 Chinese Physical Society and IOP Publishing Ltd

modulator (LCoS-SLM) for complex-amplitude modulation. Although DMD has a very fast modulation speed, DMD is a binary amplitude SLM. To achieve complex-amplitude modulation, it needs to utilize binary hologram encoding and spatial filtering techniques. Therefore, these DMD-based methods suffer from very low-phase modulation efficiency and complex optical structure. The proposed method uses LCoS-SLM for complex-amplitude modulation without any light loss, providing a relatively high modulation efficiency and a simple optical structure. Unlike DMD-based methods, which use a chessboard pattern to introduce a reference beam,[41–43] the proposed scheme directly use the unmodulated light in the LCoS reflected beam as the reference light. The single-beam structure is more compact and stable in practical application. With the help of a four-step phase-shifting, the complex-valued Fourier spectrum can be acquired by single-pixel detection. The desired complex-amplitude image can be further retrieved by applying an inverse Fourier transform. In the experiments, the proposed CFSI is implemented with three different types of objects. Experimental results demonstrate that the LCoS-SLM-based, coherent structured illumination enables the CFSI method to have high quality and a stable configuration. In addition, we find that the undersampling technique can effectively remove noise and considerably accelerate the image acquisition process in the CFSI scheme.

2. Methods

2.1. Schematic of our CFSI

The schematic of our CFSI is depicted in Fig. 1. A He–Ne laser of wavelength 632.8 nm is first expanded and collimated by a spatial filter (SF) and a collimating lens (L_1), then passes through a beam splitter (BS), and finally incident on a phase-only liquid-crystal-on-silicon spatial light modulator (LCoS-SLM). Since the modulation efficiency of the LCoS is not 100%, the reflected light consists of two parts: the phase-modulated structured light and the directly reflected light that serves as the reference light. The structured light and the reference light travel along the same path, resulting in common-path interference to form coherent structured illumination.

The coherent structured illumination is reflected by BS and imaged onto the target object (O) via a $4f$ system, which consists of two achromatic doublet lenses (L_2, L_3) with an aperture of 50 mm and focal lengths of 30 cm and 10 cm, respectively. To avoid the influence of multi-order diffracted light from the pixelated LCoS panel, the iris diaphragm (D) removes the high-order diffracted light, leaving only the zero-order diffracted light. The transmitted object light passes through a collecting lens (L_4) of focal length 30 cm and aperture 75 mm, and then reaches the single-mode fiber optic patch cable (SMF). Since O and the end face of SMF are located at the front and rear focal planes of L_4, the Fourier spectrum of the transmitted object light is obtained at the end face of the SMF. Unlike conventional SPI that directly detects the total intensity of the transmitted object light, our CFSI needs to acquire the superposition of the complex amplitude, which is exactly the zero-frequency component of the transmitted object light. Due to the core diameter of about 9 μm, only the zero-frequency component of the object spectrum can enter the SMF. A PMT detects the light from SMF, and the resulting output is fed to a PC via a data acquisition board (DAQ).

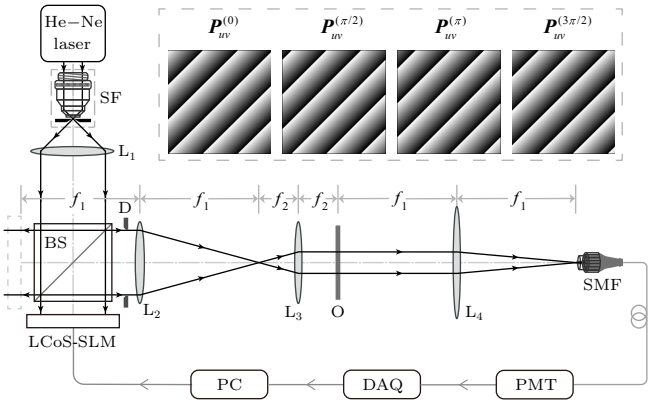


Fig. 1. Schematic of our CFSI. SF, spatial filter system; L_1, collimating lens; BS, 50:50 non-polarizing beamsplitter; LCoS-SLM, liquid-crystal-on-silicon spatial light modulator; D, iris diaphragm; L_2, L_3, achromatic doublet lenses; O, target object; L_4, collecting lens; SMF, single-mode fiber optic patch cable; PMT, photomultiplier tube; DAQ, data acquisition board; PC, personal computer.

2.2. Fourier basis scan for our CFSI

Let the spatial sampling matrix of the complex transmittance of the target object be $\boldsymbol{f}$. By definition, the two-dimensional discrete Fourier transform can be written as

$$F(u,v)=\sum_{x=0}^{M-1}\sum_{y=0}^{N-1} f(x,y)\exp\left[-\mathrm{j}2\pi\left(\frac{ux}{M}+\frac{vy}{N}\right)\right], \quad (1)$$

where $f(x,y)$ represents the element of the sampling matrix $\boldsymbol{f}$, $F(u,v)$ represents the Fourier spectrum component, and $u=0,1,\ldots,M-1$, $v=0,1,\ldots,N-1$, and M, N denote the number of rows and columns of the sampling matrix $\boldsymbol{f}$, respectively. The complete set of Fourier basis matrices can be expressed as

$$\left\{\boldsymbol{T}_{uv}\middle|\begin{array}{l}u=0,1,\ldots,\lceil M/2\rceil-1,-\lfloor M/2\rfloor,\ldots,-1,\\ v=0,1,\ldots,\lceil N/2\rceil-1,-\lfloor N/2\rfloor,\ldots,-1.\end{array}\right\}, \quad (2)$$

where the Fourier basis matrix $\boldsymbol{T}_{uv}$ is defined as

$$T_{uv}(x,y)=\exp\left[-\mathrm{j}2\pi\left(\frac{ux}{M}+\frac{vy}{N}\right)\right], \quad (3)$$

where

$$\begin{aligned}x &= -\lfloor M/2\rfloor,\ldots,-1,0,1,\ldots,\lceil M/2\rceil-1,\\ y &= -\lfloor N/2\rfloor,\ldots,-1,0,1,\ldots,\lceil N/2\rceil-1,\end{aligned}$$

where $\lfloor\cdot\rfloor$ and $\lceil\cdot\rceil$ denote floor and ceiling operations, respectively. Taking into account the periodicity of the discrete Fourier transform, the range of values of the spatial coordinates is shifted so that the origin of the coordinates lies at the

center of the matrix, and the range of values of the spatial frequency coordinates is also shifted to facilitate the inverse discrete Fourier transform (IDFT) to reconstruct the complex transmittance of the target object. Then the Fourier spectrum coefficient $F(u,v)$ can be obtained by

$$F(u,v)=\sum_{x=0}^{M-1}\sum_{y=0}^{N-1} f(x,y)T_{uv}(x,y)=\langle \boldsymbol{f},\boldsymbol{T}_{uv}^{*}\rangle_{\mathrm{F}}, \tag{4}$$

where $\langle\cdot,\cdot\rangle_{\mathrm{F}}$ denotes the Frobenius inner product, and $*$ denotes complex conjugate. Each Fourier spectrum coefficient can be acquired one by one, hence this technique is called the Fourier basis scan.

From the definition of Eq. (3), it can be seen that the Fourier basis matrix $\boldsymbol{T}_{uv}$ is a phase-only matrix with the phase distribution of $\arg\boldsymbol{T}_{uv}\in[0,2\pi)$. Using the phase distribution, we can generate a phase pattern

$$\boldsymbol{P}_{uv}=\frac{1}{2\pi}\arg\boldsymbol{T}_{uv}. \tag{5}$$

We load the LCoS with the phase pattern $\boldsymbol{P}_{uv}$ to generate the corresponding structured light, which has the form of $E_0\boldsymbol{T}_{uv}$, where E_0 is the amplitude of the structured light. The reference light can be expressed as $E_{\mathrm{r}}\mathrm{e}^{-\mathrm{j}\phi_{\mathrm{r}}}$, where E_{r} is the amplitude and ϕ_{r} is the initial phase. Thus, the coherent structured illumination has the form of

$$\boldsymbol{E}_{uv}=E_0\boldsymbol{T}_{uv}+E_{\mathrm{r}}\mathrm{e}^{-\mathrm{j}\phi_{\mathrm{r}}}\mathbf{1}, \tag{6}$$

where $\mathbf{1}$ denotes a matrix of ones which has the same dimension as $\boldsymbol{T}_{uv}$. Under this coherent structured illumination, the transmitted object light can be written as $f(x,y)E_{uv}(x,y)$. The collecting lens performs Fourier transform of the transmitted object light, and the spectrum of the object light is obtained at its back focal plane. The zero-frequency component located at the focal point can be expressed as

$$\sum_{x=0}^{M-1}\sum_{y=0}^{N-1} f(x,y)E_{uv}(x,y)=\langle \boldsymbol{f},\boldsymbol{E}_{uv}^{*}\rangle_{\mathrm{F}}. \tag{7}$$

The zero-frequency component is filtered out by SMF and then fed into the PMT. The response of the PMT can be expressed as

$$D(u,v)=\eta\,|\langle \boldsymbol{f},\boldsymbol{E}_{uv}^{*}\rangle_{\mathrm{F}}|^2, \tag{8}$$

where η represents the quantum efficiency of the PMT.

A 4-step phase shift method is used to acquire the Fourier spectrum. This requests shifting the Fourier basis matrix $\boldsymbol{T}_{uv}$ by $\varphi=0,\ \pi/2,\ \pi,\ 3\pi/2$ to obtain a set of phase-shifted basis matrices $\boldsymbol{T}_{uv}^{(\varphi)}=\mathrm{e}^{\mathrm{j}\varphi}\boldsymbol{T}_{uv}$. The corresponding phase patterns are generated by $\boldsymbol{P}_{uv}^{(\varphi)}=\arg\boldsymbol{T}_{uv}^{(\varphi)}/2\pi$, as shown in the inset of Fig. 1. We load the whole set of the phase patterns $\{\boldsymbol{P}_{uv}^{(\varphi)}\}$ onto the LCoS one by one and acquire the corresponding responses of PMT, denoted as $\{D^{(\varphi)}(u,v)\}$. Then we can retrieve the Fourier spectrum matrix of the target object from the responses of PMT as

$$\boldsymbol{F}=\alpha\left\{\left[\boldsymbol{D}^{(0)}-\boldsymbol{D}^{(\pi)}\right]+\mathrm{j}\left[\boldsymbol{D}^{(3\pi/2)}-\boldsymbol{D}^{(\pi/2)}\right]\right\}, \tag{9}$$

where α is a complex constant. By using the IDFT, we can reconstruct the complex transmittance of the target object

$$\boldsymbol{f}=\mathrm{fftshift}\big\{\mathrm{ifft2}\{\boldsymbol{F}\}\big\}, \tag{10}$$

where $\mathrm{ifft2}\{\cdot\}$ denotes the two-dimensional IDFT operation using a fast algorithm and the subsequent $\mathrm{fftshift}\{\cdot\}$ operation shifts the coordinate origin to the center of the matrix.

3. Experimental results and analysis

In all experiments, we set the imaging resolution to 128×128 pixels, and display each pixel of the phase patterns as 2×2 LCoS pixels. Since the effective aperture is large enough, all the coherent structured illumination patterns can be imaged onto the object by the $4f$ system. As the pixel pitch of the LCoS is 8 μm and the magnification of the $4f$ system is $1/3$, the spatial resolution and the field of view of this CFSI are theoretically 5.33 μm and 682.67 μm in the experiments.

As a demonstration, we first apply our CFSI to image a glass plate etched with three intersecting discs. As shown in Fig. 2(a), the discs are all 400 μm in diameter, and the circumference of each disc passes through the centers of the other two discs. The etching depths in red, green and blue regions are 372 nm, 715 nm, and 1051 nm, respectively. The phase difference introduced by etching can be expressed as $\delta\phi=2\pi(n-1)h/\lambda$, where h denotes etching depth, $\lambda=632.8$ nm is the He–Ne laser wavelength, and $n=1.457$ is the refractive index of the glass plate. Thus, relative to the unetched region, the phase of the red, green and blue regions are 0.53π, 1.03π, and 1.52π ahead, respectively. This is a simple phase object. Figure 2(b) shows the macro photo of this etched object captured by a digital camera. Figure 2(c) shows the theoretical phase distribution of this etched object, and the phase profile along the highlighted line is shown in Fig. 2(d). To clearly illustrate the phase distribution, the reconstructed phase images has been subjected to a phase-unwrapping operation.[52,53]

Figure 2(e) shows the magnitude of the measured spectrum. The values of the measured spectrums are linearly scaled to $[0,1]$, but the dynamic range of the spectrum is compressed to show the high-frequency components more clearly. The reconstructed amplitude and phase images are shown in Figs. 2(f) and 2(g), respectively, and the phase profile along the highlighted line is shown in Fig. 2(h). The values of the reconstructed amplitude images are linearly scaled to $[0,1]$ for display. Due to the phase modulation error of LCoS-SLM, external vibration and other factors, the measured spectrum contains noises, which affect the reconstructed image quality. The low-frequency noises cause a bright dot in the center of the reconstructed amplitude image, as shown in Fig. 2(f).

The high-frequency noises, which can be seen as two symmetric pairs of bright dots in the magnitude spectrum shown in Fig. 2(e), cause the reconstructed phase fluctuation, as shown in Fig. 2(h). At full sampling ratio, the number of measured basis matrices is $M = 4 \times 128 \times 128 = 65536$. Here it takes 178.5 ms to measure each basis matrix, including 100 ms to wait for the phase pattern stable display, 60 ms for intensity data acquisition, and 18.5 ms for other overheads. Thus, the total imaging acquisition time is 195 min. It should be noted that the longer the intensity data acquisition time, the better the suppression of photoelectric conversion noise and fluctuations caused by the phase flicker of LCoS-SLM in the PMT output signal.

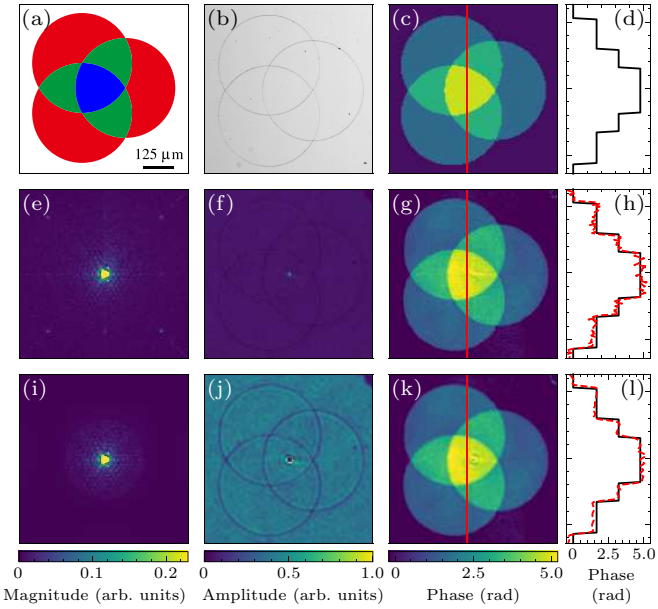


Fig. 2. The glass plate etched with three intersecting discs and related experimental results. (a) Geometry diagram of the etched discs. (b) The macro photo of the etched object. (c) The theoretical phase distribution of the etched object. (d) The phase profile along the highlighted line shown in panel (c). (e)–(h) The magnitude of the measured spectrum, the reconstructed amplitude and phase images, and the phase profile at full sampling ratio, respectively, and (i)–(l) the corresponding results at the sampling ratio of 17.2%, respectively.

The high-frequency noises can be avoided by undersampling. Since only the low-frequency coefficients are acquired during undersampling imaging under the circular sampling strategy,[54] the acquired spectrum is exactly the same as the full spectrum after ideal low-pass filtering. The smaller the sampling ratio, which corresponds to a lower cutoff frequency, the better the noise reduction, but also the more image details are lost. Here we set the sampling ratio of 17.2%, at which point the high-frequency noises basically disappears, as shown in Fig. 2(i). In addition, undersampling can significantly reduce the acquisition time. At the current sampling ratio, the total imaging acquisition time is about 34 min. To eliminate the influence of low-frequency noises, we need to perform noise suppression during image reconstruction, similar to that proposed by Xiao *et al.* in Ref. [55]. We use the subimage within the 3×3 neighborhood of the center of the reconstructed image as an estimate of the spectrum of the low-frequency noises in all experiments. The final reconstructed amplitude and phase images are shown in Figs. 2(j) and 2(k), respectively, and the phase profile along the highlighted line is shown in Fig. 2(l). It can be seen that the reconstructed image after noise reduction has clear amplitude and smooth and accurate phase.

In the second experiment, we challenge our CFSI with a detailed phase object, which is a glass plate etched with the logo of Hebei University. As shown in Fig. 3(a), the diameter of the logo is 600 μm, and the etching depths in the red, green and blue regions are 372 nm, 715 nm, and 1051 nm, respectively. Figure 3(b) shows the macro photo of this etched object captured by a digital camera. Figure 3(c) shows the theoretical phase distribution of this etched object for the light of wavelength 632.8 nm, and the phase profile along the highlighted line is shown in Fig. 3(d).

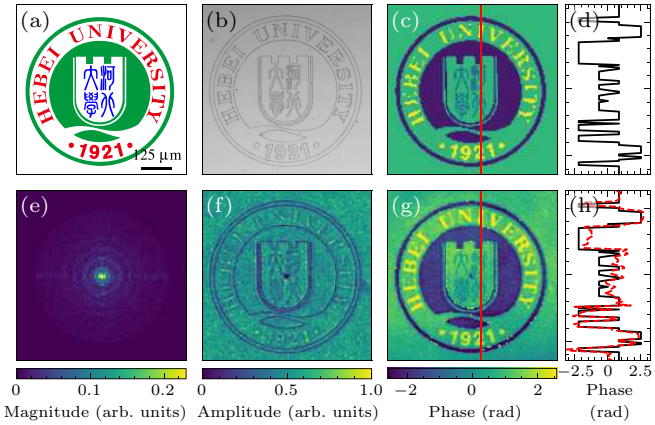


Fig. 3. The glass plate etched with the logo of Hebei University and related experimental results. (a) Geometry diagram of the etched logo. (b) The macro photo of the etched object. (c) The theoretical phase distribution of the etched object. (d) The phase profile along the highlighted line shown in panel (c). (e)–(h) The magnitude of the measured spectrum, the reconstructed amplitude and phase images, and the phase profile at the sampling ratio of 47.9%, respectively.

In this case, to preserve as much detail as possible, we set the sampling ratio to 47.9%. To further suppress noise and fluctuations in the PMT output signal, the measurement time per basis matrix is extended to 491.6 ms. Thus, the total imaging acquisition time is about 257 min. Figure 3(e) shows the magnitude of the measured spectrum. The reconstructed amplitude and phase images are shown in Figs. 3(f) and 3(g), respectively, and the phase profile along the highlighted line is shown in Fig. 3(h). It can be seen that the reconstructed amplitude image shown in Fig. 3(f) matches very well with the macro photo given in Fig. 3(b). As seen in Figs. 3(g) and 3(h) the reconstructed phase image using this CFSI are clear and accurate. However, there is a loss of some details in the reconstructed images, for example, the Chinese characters in the central region of the logo. This is due to insufficient spatial resolution in the experiment.

In the third experiment, we use a damselfly wing as the target object, to test the imaging capability of this CFSI method for natural biological tissues. We use this CFSI method to image the wing in the red box region, as shown in Fig. 4(a), and the reconstructed amplitude and phase images are shown in Figs. 4(b) and 4(c), respectively. The corresponding three-dimensional surface of the phase image is shown in Fig. 4(d). The results show that the wing is a complex-amplitude object with both an amplitude and a phase distribution. With the phase distribution, we can obtain more information about the wing. Due to less details, here we set the sampling ratio to 17.2% and the measurement time per basis matrix to 178.5 ms. Thus, the total image acquisition time is about 34 min.

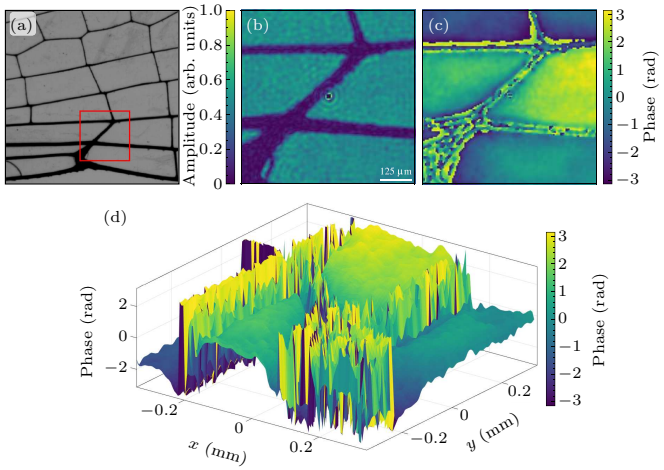


Fig. 4. The damselfly wing and related experimental results. (a) The wing photo. The red box indicates the imaging region. (b) and (c) The reconstructed amplitude and phase images, respectively, at the sampling ratio of 17.2%. (d) The corresponding three-dimensional surface of the phase image (c).

Due to vibration, lens aberrations, etc. the achievable spatial resolution is larger than the theoretical value of 5.33 μm in practice. In the fourth experiment, we use the negative USAF-1951 resolution test chart as the target object to quantify the achievable spatial resolution in the experiments. The experimental results are shown in Fig. 5, where (a) and (b) show the amplitude image and phase image, respectively. The amplitude profiles along the highlighted lines across the horizontal and vertical bars of group 6 element 3 are shown in the left and top subplots, respectively, where the axes along the image represent the pixel positions and each dot represents the amplitude value of one pixel. The corresponding phase profiles are also given in Fig. 5(b). As shown in Fig. 5(a), group 6 element 3 can be clearly resolved. This means that the achievable spatial resolution is about 6.2 μm. Since the resolution test chart is an amplitude-only object, the phase of all transmissive regions is consistent, however, the phase in the opaque region is severely contaminated by noise and shows large fluctuations, as shown in Fig. 5(b). Therefore, the reconstructed phase image does not look good enough. In this case, we set the sampling ratio to 62.2% and the measurement time per basis matrix to 491.6 ms. Thus, the total imaging acquisition time is about 334 min.

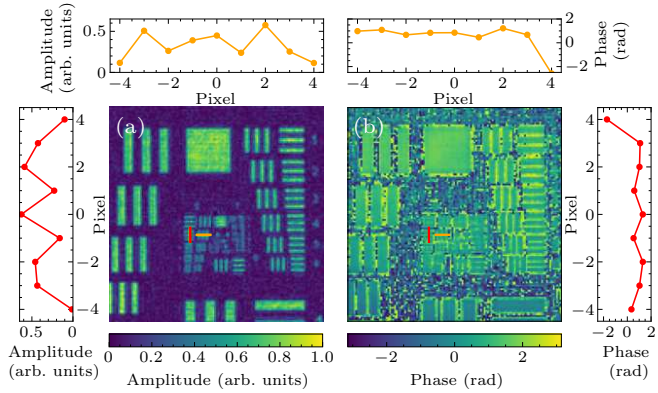


Fig. 5. Experimental results of the USAF-1951 resolution test chart. (a) and (b) The reconstructed amplitude and phase images, respectively at the sampling ratio of 62.2%. The four subplots show the amplitude and phase profiles along the highlighted lines across the horizontal and vertical bars of group 6 element 3, respectively.

The above three sets of experimental results illustrate that the proposed CFSI approach can be applied to a variety of different types of objects. Although the current optical setup is constructed for measuring a transmissive object, it can be easily changed for measuring a reflective object. Combined with undersampling and noise suppression techniques, reconstructed images are clear and accurate. It should be noted that undersampling can cause the reconstructed image to lose some details while reducing high-frequency noise. Therefore, the sampling ratio needs to be traded off to obtain the best reconstructed image. At a certain sampling ratio, the spatially non-uniform sampling technique[56] may be able to obtain images with richer details. In addition, there is another main challenge remaining for further pursuit. Limited by the response speed and the phase flicker of our LCoS-SLM, the total imaging acquisition time is very long. Therefore, the present method can only be used to observe stationary objects. The most straightforward way to address this issue is to use a faster response LCoS-SLM with less phase flicker. In addition, this issue can also be tackled by adopting the more efficient three-step phase-shifting technique,[40] or non-phase-shifting techniques such as off-axis holography.[57]

4. Conclusion

In summary, we propose and experimentally demonstrate a novel complex-amplitude imaging method. By utilizing a phase-only SLM to generate coherent Fourier basis patterns as illumination, we can use a single-pixel detector to acquire the complex-valued Fourier spectrum of an object. In combination with the undersampling technique and noise suppression, we can recover a high-quality complex-amplitude image of the object. In experiments, we implement this CFSI method with two etched glass objects, a damselfly wing, and a resolution

test chart. The reconstructed complex-amplitude images have clear amplitude, accurate phase and spatial resolution of up to 6.2 μm. In addition, due to the use of common-path interference, the experimental configuration of this CFSI is compact and stable, which is readily integrated into commercial microscopes for quantitative phase microscopy. Thus, this complex-amplitude imaging method might find broad applications in optical metrology and biomedical science, especially for the cases with a light of invisible wavelength or extremely low intensity.

Data availability

Data underlying the results presented in this paper are available in Dataset (Ref. [58]).

Acknowledgments

The authors are grateful to Huan Zhou for her helpful discussions and suggestions. Project supported by the Natural Science Foundation of Hebei Province, China (Grant Nos. A2022201039 and F2019201446), the Multi-Year Research Grant of University of Macau, China (Grant No. MYRG2020-00082-IAPME), the Science and Technology Development Fund from Macau SAR (FDCT), China (Grant No. 0062/2020/AMJ), the Advanced Talents Incubation Program of the Hebei University (Grant No. 8012605), and the National Natural Science Foundation of China (Grant Nos. 11204062, 61774053, and 11674273).

References

[1] Zernike F 1942 *Physica* **9** 686
[2] Preza, C, Snyder, D L and Conchello J A 1999 *J. Opt. Soc. Am. A* **16** 2185
[3] Platt B C and Shack R 2001 *Journal of Refractive Surgery* **17** S573
[4] Miao J, Charalambous P, Kirz J and Sayre D 1999 *Nature* **400** 342
[5] Fu J and Li P 2013 *Chin. Phys. B* **22** 014204
[6] Marquet P, Rappaz B, Magistretti P J, Cuche E, Emery Y, Colomb T and Depeursinge C 2005 *Opt. Lett.* **30** 468
[7] Li T, Lei W X, Sun X K, Dong J, Tao Y and Shi Y S 2021 *Chin. Phys. B* **30** 094201
[8] Zheng G, Horstmeyer R and Yang C 2013 *Nat. Photon.* **7** 739
[9] Zhang D J, Tang Q, Wu T F, Qiu H C, Xu D Q, Li H G, Wang H B, Xiong J and Wang K 2014 *Appl. Phys. Lett.* **104** 121113
[10] Yu H, Lu R, Han S, Xie H, Du G, Xiao T and Zhu D 2016 *Phys. Rev. Lett.* **117** 113901
[11] Zhao Y N, Zhang S H, Cui W L, Cao D Z and Liang B L 2021 *Journal of Optics* **23** 055603
[12] Zuo C, Li J, Sun J, Fan Y, Zhang J, Lu L, Zhang R, Wang B, Huang L and Chen Q 2020 *Optics and Lasers in Engineering* **135** 106187
[13] Gibson G M, Johnson S D and Padgett M J 2020 *Opt. Express* **28** 28190
[14] Edgar M P, Gibson G M, Bowman R W, Sun B, Radwell N, Mitchell K J, Welsh S S and Padgett M J 2015 *Scientific Reports* **5** 10669
[15] Stantchev R I, Yu X, Blu T and Pickwell-MacPherson E 2020 *Nat. Commun.* **11** 2535
[16] Duan D and Xia Y 2021 *Opt. Express* **29** 4978
[17] He Y H, Zhang A X, Li M F, Huang Y Y, Quan B G, Li D Z, Wu L A and Chen L M 2020 *APL Photonics* **5** 056102
[18] Li Z, Suo J, Hu X, Deng C, Fan J and Dai Q 2017 *Scientific Reports* **7** 41435
[19] Zhao Y N, Hou H Y, Han J C, Liu H C, Zhang S H, Cao D Z and Liang B L 2021 *Opt. Lett.* **46** 4900
[20] Kirmani A, Venkatraman D, Shin D, Colaço A, Wong F N C, Shapiro J H and Goyal V K 2014 *Science* **343** 58
[21] Liu X, Shi J, Sun L, Li Y, Fan J and Zeng G 2020 *Opt. Express* **28** 8132
[22] Sun M J, Edgar M P, Gibson G M, Sun B, Radwell N, Lamb R and Padgett M J 2016 *Nat. Commun.* **7** 12010
[23] Ma Y, Yin Y, Jiang S, Li X, Huang F and Sun B 2021 *Optics and Lasers in Engineering* **140** 106532
[24] Li X, Meng X, Yang X, Wang Y, Yin Y, Peng X, He W, Dong G and Chen H 2018 *Optics and Lasers in Engineering* **102** 106
[25] Wang Y, Liu Q, Wang J and Wang Q H 2018 *Chin. Phys. B* **27** 034202
[26] Zheng P, Dai Q, Li Z, Ye Z, Xiong J, Liu H C, Zheng G and Zhang S 2021 *Science Advances* **7** eabg0363
[27] Lee K and Ahn J 2010 *Appl. Phys. Lett.* **97** 241101
[28] Horisaki R, Matsui H, Egami R and Tanida J 2017 *Appl. Opt.* **56** 1353
[29] Horisaki R, Matsui H and Tanida J 2017 *Appl. Opt.* **56** 4085
[30] Howland G A, Lum D J and Howell J C 2014 *Opt. Express* **22** 18870
[31] Shin S, Lee K, Baek Y and Park Y 2018 *Phys. Rev. Applied* **9** 044042
[32] Soldevila F, Durán V, Clemente P, Lancis J and Tajahuerce E 2018 *Optica* **5** 164
[33] Li M, Bian L, Zheng G, Maiden A, Liu Y, Li Y, Suo J, Dai Q and Zhang J 2021 *Opt. Lett.* **46** 1624
[34] Clemente P, Durán V, Tajahuerce E, Andrés P, Climent V and Lancis J 2013 *Opt. Lett.* **38** 2524
[35] Martínez-León L, Clemente P, Mori Y, Climent V, Lancis J and Tajahuerce E 2017 *Opt. Express* **25** 4975
[36] González H, Martínez-León L, Soldevila F, Araiza-Esquivel M, Lancis J and Tajahuerce E 2018 *Opt. Express* **26** 20342
[37] Hu X, Zhang H, Zhao Q, Yu P, Li Y and Gong L 2019 *Appl. Phys. Lett.* **114** 051102
[38] Santos-Amador A, Araiza-Esquivel M, González H, Rodríguez-Cobos A, Tajahuerce E, Martínez-León L, Ramírez-Flores G and Balderas-Navarro R E 2021 *Appl. Opt.* **60** 6935
[39] Wu D, Luo J, Huang G, Feng Y, Feng X, Zhang R, Shen Y and Li Z 2021 *Nat. Commun.* **12** 4712
[40] Liu Y, Suo J, Zhang Y and Dai Q 2018 *Opt. Express* **26** 32451
[41] Liu R, Zhao S, Zhang P, Gao H and Li F 2019 *Appl. Phys. Lett.* **114** 161901
[42] Zhao S, Liu R, Zhang P, Gao H and Li F 2019 *Opt. Lett.* **44** 3278
[43] Zhao S, Chen S, Wang X, Liu R, Zhang P, Li H, Gao H and Li F 2020 *Opt. Lett.* **45** 5990
[44] Liu Y, Yu P, Hu X, Wang Z, Li Y and Gong L 2020 *Opt. Lett.* **45** 4028
[45] Li X, Sun Y, He Y, Li X and Sun B 2021 *Signal Processing* **188** 108173
[46] Hou H Y, Zhao Y N, Han J C, Cui S W, Cao D Z, Liu H C, Zhang S H and Liang B L 2021 *Opt. Express* **29** 41827
[47] Zhang Z, Ma X and Zhong J 2015 *Nat. Commun.* **6** 6225
[48] Huang J, Shi D, Yuan K, Hu S and Wang Y 2018 *Opt. Express* **26** 16547
[49] Zhang Z, Liu S, Peng J, Yao M, Zheng G and Zhong J 2018 *Optica* **5** 315
[50] Liang Z Y, Cheng Z D, Liu Y Y, Yu K K and Hu Y D 2019 *Chin. Phys. B* **28** 064202
[51] Peng J, Yao M, Huang Z and Zhong J 2021 *APL Photonics* **6** 046102
[52] Herráez M A, Burton D R, Lalor M J and Gdeisat M A 2002 *Appl. Opt.* **41** 7437
[53] van der Walt S, Schönberger J L, Nunez-Iglesias J, Boulogne F, Warner J D, Yager N, Gouillart E and Yu T 2014 *PeerJ* **2** e453
[54] Zhang Z, Wang X, Zheng G and Zhong J 2017 *Opt. Express* **25** 19619
[55] Xiao Y, Zhou L and Chen W 2019 *IEEE Photonics Technology Letters* **31** 845
[56] Phillips D B, Sun M J, Taylor J M, Edgar M P, Barnett S M, Gibson G M and Padgett M J 2017 *Science Advances* **3** e1601782
[57] Yoneda N, Saita Y and Nomura T 2022 *Opt. Express* **30** 18134
[58] Zhao Y N, Hou H Y, Han J C, Cao D Z, Zhang S H, Liu H C and Liang B L 2022 *figshare. Dataset*